WILEY-VCH

RESEARCH ARTICLE

A Three-Tiered Golf Anode towards Ultralong-Life Zn-Mn Aqueous Batteries **

Qiang Hu, Xinrui Wang, Jiuzhi Cui, Jiabing Hou, Xingquan Liu, Jia-Lin Yang, Zhen-Yi Gu, Jingxin Zhao,* Bingang Xu,* and Xing-Long Wu**

Abstract: *Zn-Mn aqueous batteries (ZMABs) are widely recognized as a promising candidate for large-scale energy storage due to their cost-effectiveness, high safety and environmental friendliness. However, the practical application of ZMABs is hindered by inherent electrical contact loss, hydrogen evolution and dendrite growth on traditional anodes. Here, a three-tiered golf anode with high conductivity is developed to simultaneously enhance the reversibility of Zn and Mn metals. The three-tiered golf anode is achieved by inner zinc powder, intermediate carbon and outer bismuth layer, which can effectively enhance the Gibbs free energy and mitigate the volume change of the anode, thus enabling stable Zn-Mn cycling. As a proof of concept, Zn-Mn full cells (coupled to CNT@MnO_2) achieve an ultralong cycle life with 94.6% capacity retention at 2 A g^{-1} after 16,000 cycles. This study presents valuable insights into the structural design of anodes aimed at enhancing the stability and durability of ZMABs.*

Introduction

Since the dawn of the 21st century, the escalating energy crisis has spurred significant advancements in the research and development of alkali metal batteries.[1-3] However, their inherent safety concerns and high costs have hindered widespread adoption. In contrast, Zn-Mn aqueous batteries (ZMABs) have garnered considerable attention due to their superior safety and economic viability. Nevertheless, the current major challenges include the formation of dendrites, the presence of dead zinc, and corrosion reactions. Currently, zinc foil is predominantly employed as the anode material for ZMABs. However, its practical application in industry is limited due to the low utilization efficiency and inherent complexities in preparation.[4,5] The utilization of zinc powder (ZP) as an anode in ZMABs is highly favored owing to its cost-effectiveness, excellent processability, and adjustable properties.[6,7] Nevertheless, compared with zinc foil, the surface area of ZP is significantly increased, and the solid spherical structure renders the zinc anode more intricate and challenging to manipulate. The ZP anodes are susceptible to uncontrolled electrical contact loss due to prolonged and uneven stripping, which causes the active substance to separate from the electrode (Figure 1a), thus resulting in increased battery polarization and poor coulomb efficiency (CE).[8] Moreover, the ZP anode is susceptible to dendrite growth, hydrogen evolution reaction (HER), and heterogeneous deposition of Zn-Mn during the cycle of ZMABs due to its low Young's modulus, high ion transport barrier and susceptibility to corrosion in the aqueous electrolyte[9, 10]. Therefore, the development of stable and long-lasting ZP anodes is crucial for enhancing the cycling performance of ZMABs.

The challenges associated with dendrite growth and electrical contact failure on the surface of ZP anode have been effectively addressed through the implementation of various strategies, including advanced coating techniques for ZP,[11] precise regulation of electrolyte solvation,[12] and optimization of structural design for the anode.[13] At present, the research of ZP anode is still in the initial stage, and the further development of its application potential and research value in ZMABs is warranted. Additionally, the spherical structure of the ZP anode makes it more susceptible to uneven deposition during the plating process of Zn^{2+}, ultimately leading to dendrite formation and subsequent short circuits.[14,15] To overcome these challenges, a variety of high-conductivity materials such as MXene,[16] graphene,[17] and ZnBi alloys,[18] were employed in the ZP anode to achieve uniform deposition of Zn^{2+} and prevent electrical contact failure. To achieve effective homogenization of the Zn^{2+} flux and deceleration of the Zn deposition rate during anode cycling, a 3D cold trap environmental printing technique was proposed for attaining highly ordered MXene and ZP anodes.[19] Additionally, Wang et al. fabricated in situ carbon mesh anodes by applying a grape sugar coating to ZP.[20] This carbon network establishes a continuous internal pathway for electron transport and optimizes the distribution of surface electric fields, resulting in highly reversible zinc deposition. Besides, to mitigate the corrosion and dendrite formation of ZP, an ultra-stable ZP-based anode was fabricated through 3D printing and coated with a conformal conductive hydrogel layer.[21] The cross-linked hydrogels can redistribute the flux of Zn^{2+}, and the 3D structure reduces the stress caused by volume change at high current density or high capacity. Obviously, these multifunctional materials for ZP-based anodes have demonstrated the ability to mitigate electrical contact loss and dendrite growth of ZP. However, it is worth noting that the average size of the utilized ZP still remains relatively large (> 15 μm). Additionally, the enhanced conductivity of modified ZP-based anodes promotes HER, which in turn contributes to potential failure and gas generation risks in aqueous batteries.

Here, the Zn@C double-layer composite anode was initially fabricated using a powder sherardizing strategy, wherein molten zinc powder liquid was utilized as the solvent and carbon spheres served as the solute. The incorporation of commercial zinc powder within the carbon sphere enhances both the conductivity and specific surface area of the anode; however, it concurrently promotes HER. Therefore, we employed the liquid phase reduction method to deposit a small quantity of bismuth metal onto Zn@C and unmelted zinc powder, which effectively suppress gas generation. The resulting final product comprises of Zn metal, C spheres, and Bi metal powder, and the three-

[*] Dr. Q. Hu, X. Wang, J. Cui, J. Hou, Prof. X. Liu
School of Materials and Energy, University of Electronic Science and Technology of China, Chengdu 610054, P. R. China.
E-mail: Lxquan@uestc.edu.cn
Dr. J. Zhao, Prof. B. Xu
Nanotechnology Center, School of Fashion and Textiles, The Hong Kong Polytechnic University, Hung Hom, Kowloon, Hong Kong, 999077, P. R. China.
E-mail: JingxinZhao@tju.edu.cn; tcxubg@polyu.edu.hk
Dr. J. L. Yang, Z. Y. Gu, Prof. X. L. Wu
MOE Key Laboratory for UV Light-Emitting Materials and Technology, Northeast Normal University, Changchun 130024, P. R. China.
E-mail: xinglong@nenu.edu.cn

[**] Supporting information for this article is given via a link at the end of the document.

tiered golf anode is designated as ZCBP. As illustrated in Figure 1b, the ZCBP anode can effectively inhibit HER and regulate Zn/Mn metal reversibility by providing the electrode with superconductivity, tight electrical contact, enhanced Gibbs free energy, and anti-corrosion characteristics. Additionally, the three-tiered golf anode characterized by a low Zn^{2+} transport barrier ensure the preferential deposition of Zn(002), effectively inducing a planar deposition model and thus inhibiting the formation of zinc dendrites. As a result, the as-fabricated ZCBP symmetric cells deliver excellent cyclic stability of 5,000 h and an ultrahigh cumulative plated capacity (CPC) of 5 Ah cm^{-2} at 1 mA cm^{-2}/0.5 mAh cm^{-2}. More encouragingly, the ZCBP//CNT@MnO_2 cells achieve ultralong cycle life with a capacity retention of 94.6 % at 2 A g^{-1} after 16,000 cycles. Furthermore, the ZCBP/CNT@MnO_2 cells exhibit a capacity retention of 97.0 % and maintain a specific capacity of 301 mAh g^{-1} even after undergoing 100 cycles at 0.2 A g^{-1}. The rational design of ZP-based anode and the proposed powder sherardizing strategy present a novel concept for the application of ZMABs.

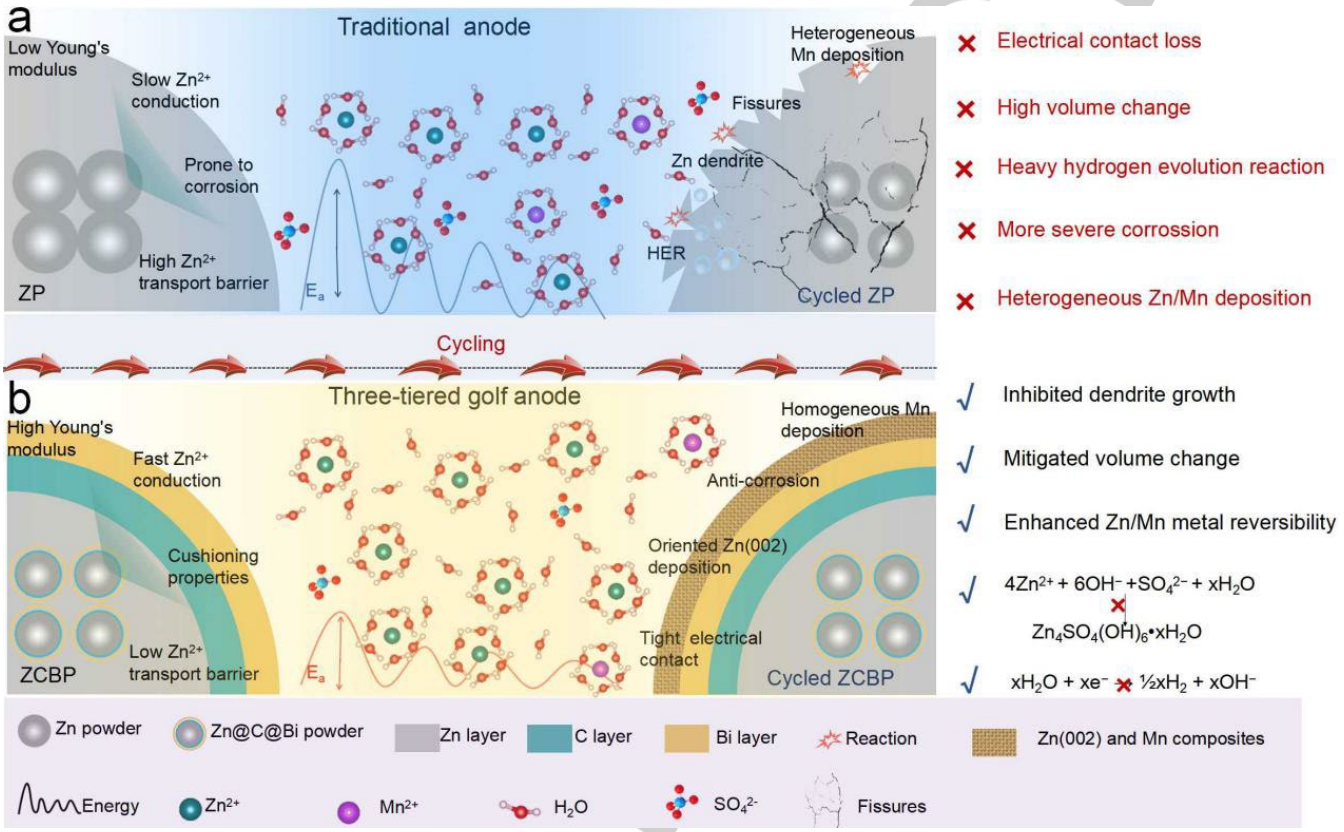

Figure 1. Schematic diagram illustrating the enhanced strengthening mechanism of the three-tiered golf anode in comparison to traditional Zn powder anode.

Results and discussion

The preparation process of ZCBP anode is shown in Figure 2a. Firstly, the precursor of zinc citrate microspheres is subject to carbonization and subsequent removal of zinc oxide, resulting in the formation of carbon microspheres while preserving the yolk-shell structure. Subsequently, the ZP is incorporated into the yolk-shell carbon microspheres via the powder sherardizing strategy at high temperature, leading to the formation of composite Zn@C powder (ZCP). Finally, the reduction of Bi^{3+} to form Bi nanosheets is achieved through liquid phase reduction method on the surface of ZCP. The X-ray diffraction (XRD) patterns unequivocally demonstrate the successful synthesis of ZCP and ZCBP (Figure S1). The microstructures of the samples were analyzed using scanning electron microscopy (SEM) and transmission electron microscopy (TEM). The yolk-shell CP is composed of elements C, N, and O (Figure 2b and Figure S2a and S3a). The CP and ZP were fused at high temperatures to form a solid ZCP; however, incomplete melting of a portion of the larger-sized ZP may hinder the achievement of a homogeneous zinc anode (Figure 2c and Figure S2b and S3b). The ZCBP is composed of a small number of Bi nanosheets and ZCP, and the Bi nanosheets is distributed across the surface of ZCP (Figure 2d and Figure S2c and S3c). Besides, the surfaces of some incompletely melted ZP are also coated with Bi nanosheets, which can facilitate the inhibition of HER in zinc anodes (Figure 2e and Figure S3d).[22] The interface region between the solid sphere and the nanosheet was observed using high resolution transmission electron microscopy (HRTEM). It is determined that region 2 predominantly consists of the (012) and (104) crystal planes of the Bi metallic phase. The presence of the solid sphere in area 1 prevents clear lattice fringes from being captured in HRTEM. The defects, elemental composition and electron states of the samples are further characterized using Raman spectroscopy and X-ray photoelectron spectroscopy (XPS). The Raman bands observed at 92.8 and 311.9 cm^{-1} can be attributed to the presence of Bi metal (Figure S4), which is consistent with the findings from XRD analysis when compared with ZP. Besides, the presence of the prominent Bi 4f peak

further substantiates the incorporation of Bi metal (Figure S5a and b). In addition, the I_D/I_G values of CP, ZCP, and ZCBP are 1.03, 0.89, and 0.87, respectively (Figure 2g), indicating a reduction in defect levels following the incorporation of zinc powder into carbon spheres. Interestingly, the ZCP sample exhibits a π-π* transition peak at 293.8 eV (Figure 2h), revealing the charge interaction between zinc and carbon atoms. To demonstrate this, the electronic conductivity of the prepared ZP and ZCP electrodes was measured. The electrical conductivity values for ZP and ZCP are 3.84 and 43.67 mS mm^{-1}, respectively (Figure 2i), indicating that ZCP exhibits excellent electron transport capacity. Similarly, the incorporation of Bi metal into the surface layer alters the binding energy of Zn atoms (Figure S5c), which could potentially enhance the electrochemical performance of the composite anode.

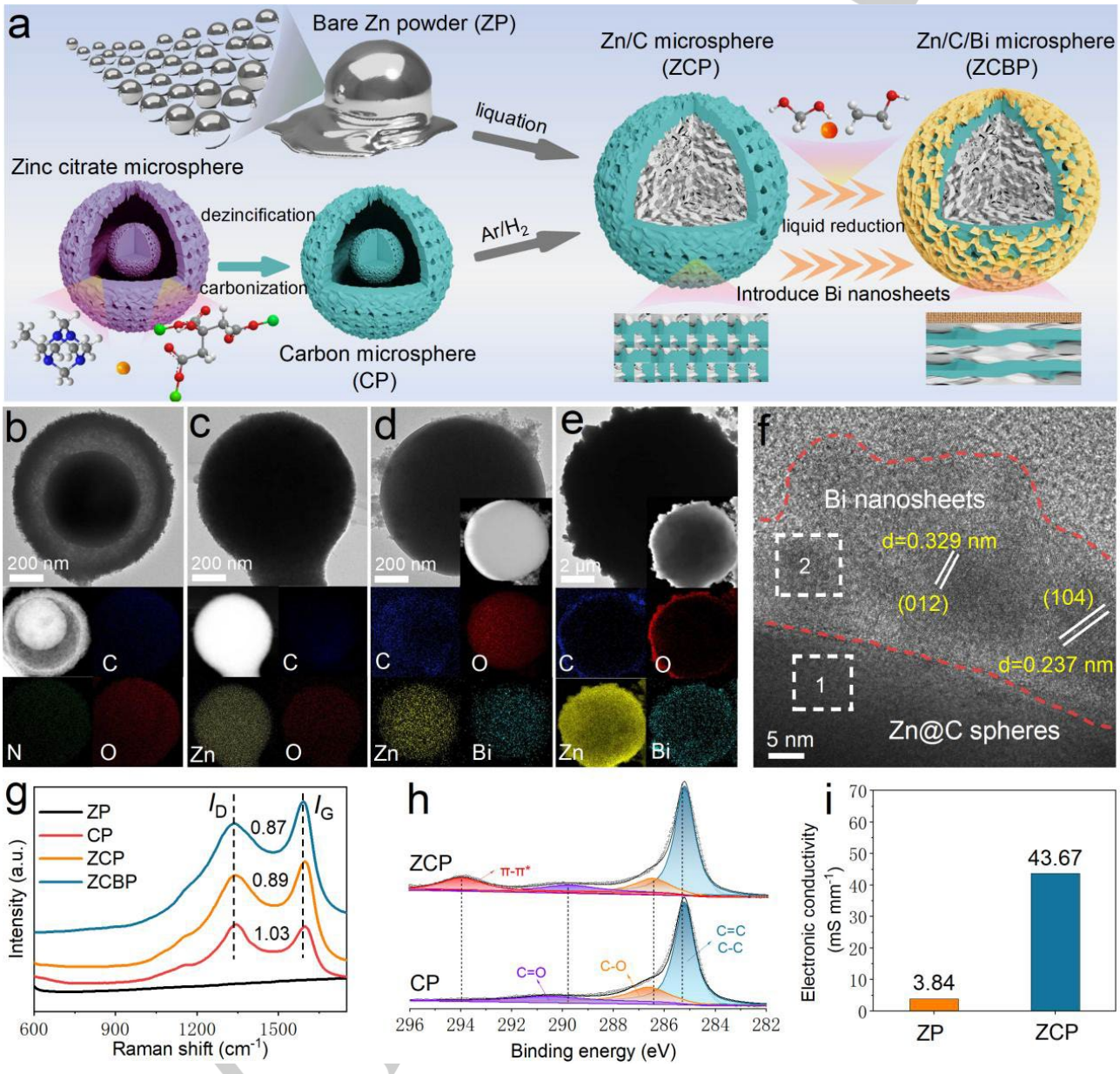

Figure 2. a) Schematic diagram of the fabrication processes. TEM and corresponding elemental mapping images of **b)** CP, **c)** ZCP and **d,e)** ZCBP. **f)** HRTEM images of ZCBP. **g)** Raman spectroscopy of the ZP, CP, ZCP and ZCBP. **h)** XPS spectra of the CP and ZCP. **i)** Electrical conductivity of ZP and ZCP electrode.

The wettability of ZP, ZCP, and ZCBP in the electrolyte is measured to be 106°, 142° and 129°, respectively (Figure S6), suggesting that the recombination of ZP and CP leads to a reduction in electrode wettability due to the hydrophobicity of carbon. Besides, the application of a Bi metal coating enhances the electrode's wettability, which may promote uniform deposition on the surface of the zinc anode. As a result, the ZCBP electrode exhibits a lower nucleation overpotential (21.1 mV) compared to that of the ZCP electrode (26.9 mV), as shown in Figure 3a. Additionally, the ZP electrode delivers higher nucleation overpotential (49.6 mV) due to the uneven particles and poor electrical contact. To validate the conclusions drawn from the aforementioned experiments, the interaction behavior between various candidate zinc anodes and Zn^{2+} was investigated through quantum chemical calculations. The binding energy results clearly indicate that

the adsorption energies (E_{ads}) of Zn-Zn, Zn-C, and Zn-Bi are −4.62, −4.83, and −16.79 kcal mol^{-1}, respectively (Figure 3b), revealing the zincophilic properties of Bi metal. Furthermore, the interfacial charge density differences (Figure 3c) and Bard charges (Figure 3d) calculations were employed for the analysis of surface atom charge transfer. The electron donation of Zn to Zn, C, and Bi surfaces is observed to be 0.003, 0.019, and 0.022 e, respectively, which suggests the more delocalized and stronger electronic interaction between Zn^{2+} and Bi. The impact of the electrode material on HER was assessed based on Gibbs free energy difference ΔG_{H^*} of H adsorption, which is widely recognized as the primary parameter for evaluating the reactivity evolution of H_2. The Bi substrate exhibits a higher ΔG_{H^*} value (0.99 eV) than that of the Zn substrate (0.72 eV), indicating a more favorable HER inertization profile (Figure 3e). The ΔG_{H^*} value increases from 0.72 to 0.82 eV after doping Bi metal onto the Zn substrate (Figure 3f), effectively demonstrating that the introduction of Bi suppresses HER on the zinc anode. Linear sweep voltammetry (LSV) curves are widely used conventional characterization technique for evaluating the performance of HER on an electrode. When the current density is 5 mA cm^{-2} (Figure 3g), the ZCBP electrode introduced with Bi metal exhibits a significant increase in overpotential (134 mV difference), indicating improved suppression of hydrogen gas during plating/stripping, which aligns with the aforementioned theoretical characterizations. Besides, the Gibbs free energy of carbon is higher compared to that of zinc and bismuth (Figure S7), suggesting its potential to suppress hydrogen evolution. However, the integration of commercial zinc powder into the carbon sphere not only enhances the conductivity and specific surface area of the anode but also increases the probability of water molecules coming into contact with the zinc anode. Since the HER occurs on the surface of the material, the morphology and structure of the material surface can influence HER more than the intrinsic properties of the material. The voltage distribution of symmetric cells at different current densities ranging from 0.5 to 5 mA cm^{-2} is compared in Figure 3h and Figure S8. The ZCBP symmetric cells demonstrate a relatively flat and symmetrical voltage platform, ensuring an extended cycle life due to their high electroactive surface area and reduced nucleation barrier.

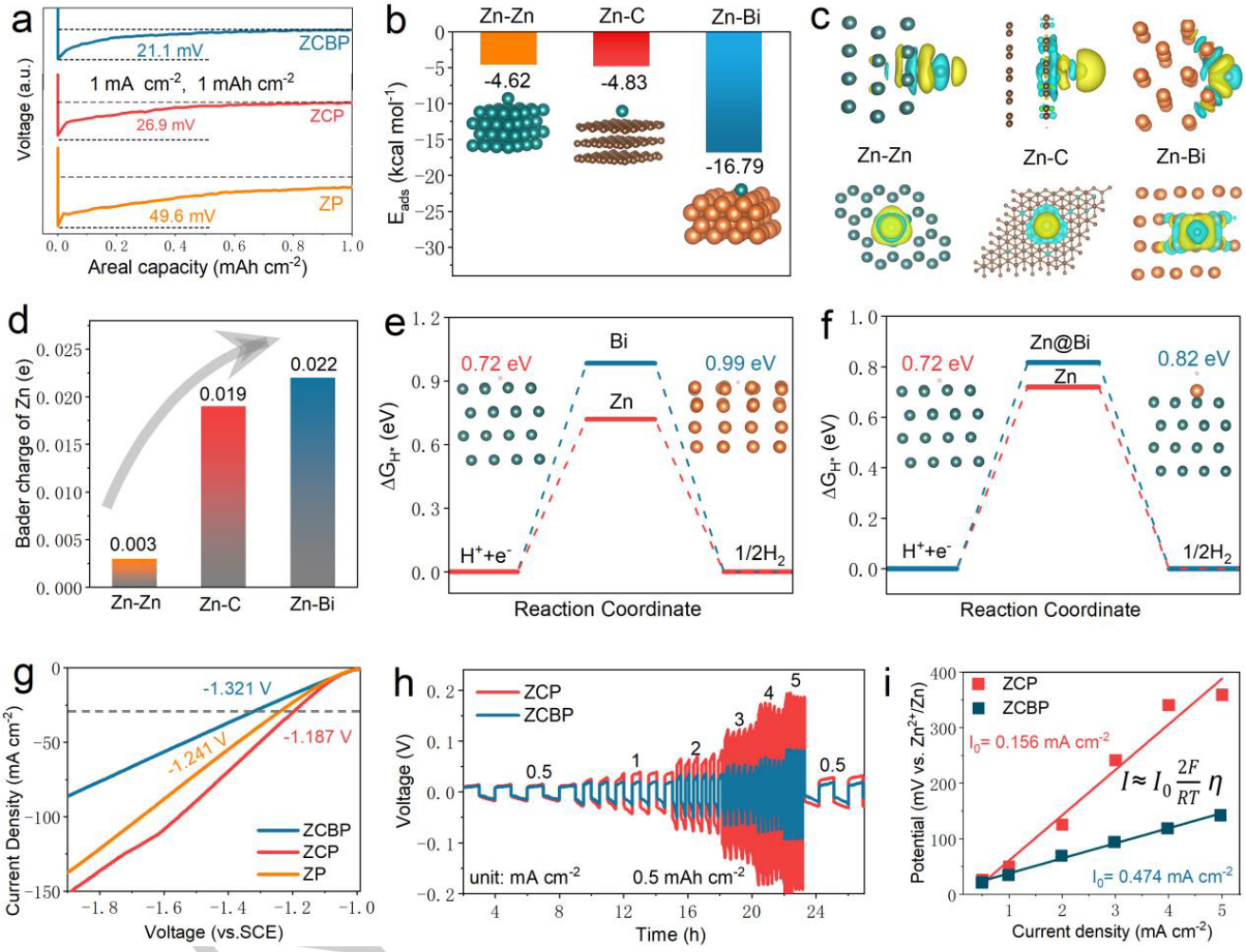

Figure 3. a) Polarization curves of Zn deposition for the ZP, ZCP and ZCBP anodes at 1 mA cm^{-2} with an areal capacity of 1 mAh cm^{-2}. **b)** Binding energies of Zn-Zn, Zn-C and Zn-Bi and the corresponding structures. **c)** The charge density difference of Zn-Zn, Zn-C and Zn-Bi (clusters with a semi-transparent yellow hue indicate an elevation in electron density, while those with a blue shade suggest a reduction). **d)** Electron donations of a Zn atom on the Zn-Zn, Zn-C and Zn-Bi substrates. **e)** ΔG_{H^*} and adsorption configurations of a H atom on the Zn-H and Bi-H substrates. **f)** ΔG_{H^*} and adsorption configurations of a H atom on the Zn-H and Zn@Bi-H substrates. **g)** LSV curves at 5 mV s^{-1} for the ZP, ZCP and ZCBP anodes. **h)** voltage profiles of ZCP//ZCP and ZCBP//ZCBP symmetric cells at various current densities from 0.5 to 5 mAcm^{-2}. **i)** Arrhenius curves of ZCP//ZCP and ZCBP//ZCBP symmetric cells.

The exchange current density is another crucial indicator that characterizes the kinetics of the redox reaction at the equilibrium potential on the electrode. For Zn electrodeposition under various current densities, Figure 3i presents the calculation formula for i_0 (based on the Butler-Volmer equation). The value of i_0 generally relies primarily on the ambient temperature, surface morphology, and hydrogen concentration.[23,24] The linear fitting analysis reveals that the i_0 value of ZCBP (0.474 mA cm^{-2}) significantly exceeds that of ZCP (0.156 mA cm^{-2}), thus confirming the inherent advantages associated with the introduction of Bi metal, which induces zinc deposition. To further validate the electrode stability, the assembled ZCP//ZCP symmetric cells exhibit a sudden increase in polarization after 1400 h of cycling, which is attributed to prolonged gas evolution within the battery (Figure S9). The assembled ZCBP//ZCBP symmetric cells achieve stable cycling for 1800 h at 2 mA cm^{-2}/1 mAh cm^{-2}, demonstrating that the incorporation of Bi metal enhances the stability of the Zn anode. The differences between ZP and ZCBP anodes during plating/stripping were further evaluated through a series of experimental and theoretical characterizations. For the ZP anode, after plating 20 min, zinc protrusions were observed to accumulate on the surface of ZP (Figure S10). Upon magnification, these protrusions are identified as by-products and flaked zinc (Figure 4a). The protrusions induce charge and ion accumulation through the "tip effect",[25] leading to gradual enlargement, thus causing uneven deposition and dendrite growth on the electrode surface. Additionally, the disorderly and loosely deposited topography will exacerbate the battery's side reaction, leading to significant changes in its volume, resulting in reduced CE and poor cycle life. For the ZCBP anode, Zn displays a more uniform growth pattern on the surface, with a preference for layer-by-layer deposition, resulting in the formation of (002)-textured Zn plating (Figure 4b). The deposition morphology remains dense even after a prolonged plating time of 80 min, with no evident presence of Zn dendrites or by-products detected.

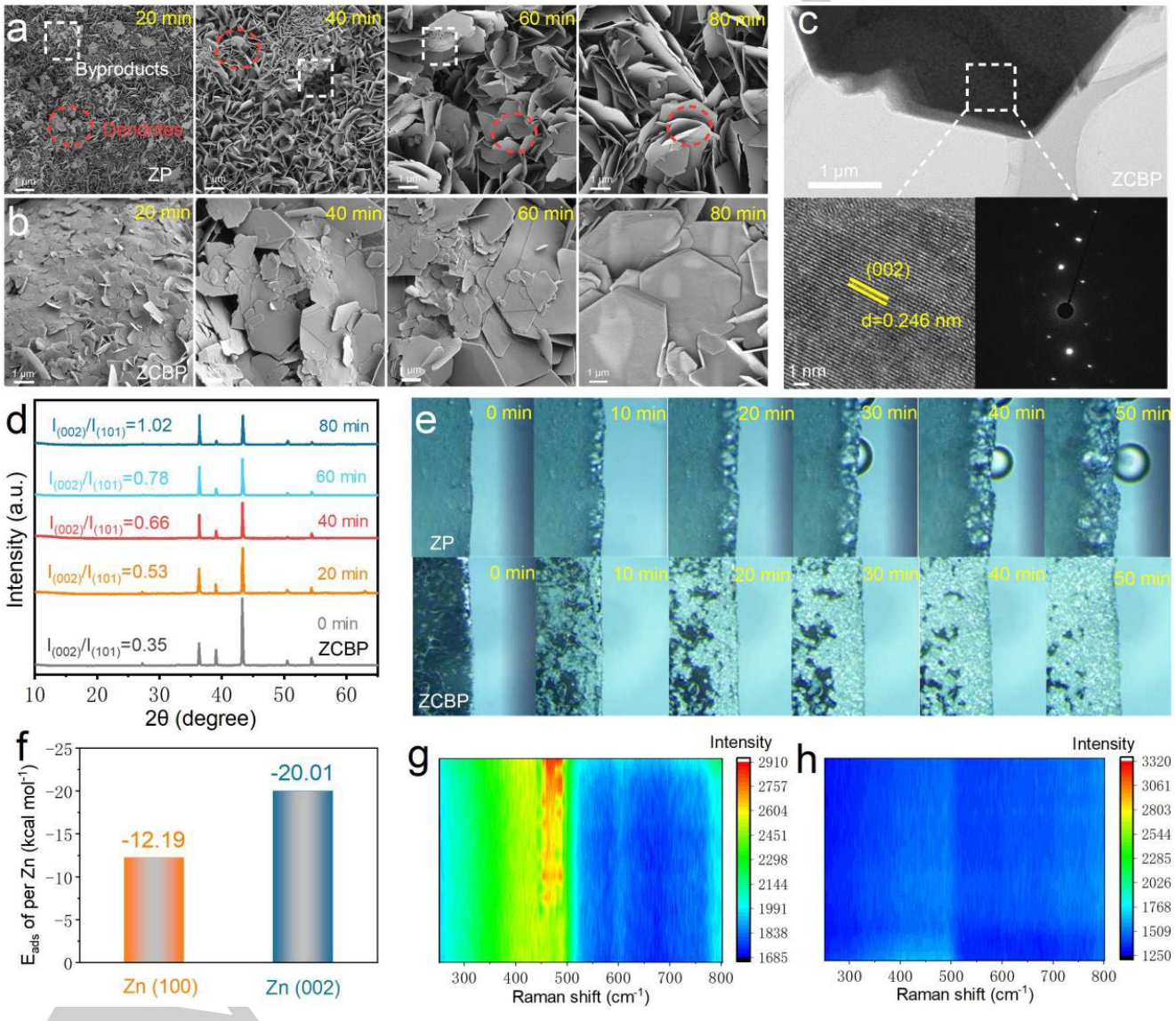

Figure 4. SEM images of **a)** ZP and **b)** ZCBP anodes after plating 20, 40, 60 and 80 min. **c)** HRTEM images and SAED patterns of ZCBP after plating 80 min. **d)** XRD patterns of ZCBP anode after plating 20, 40, 60 and 80 min. **e)** In situ optical micrographs of ZCBP deposition process. **f)** The calculated adsorption energy per Zn atom of the (100) surface and (002) surface on the Bi metal. In situ Raman spectra of **g)** ZP and **h)** ZCBP electrodes after 24 h cycling at 5 mA cm^{-2}.

HRTEM and bright-field transmission electron microscopy (BFTEM) were conducted to further determine the crystal structure of the deposited Zn. After plating for 80 min, the ZCBP displays a distinct hexagonal lamellar structure (Figure 4c). The (002) crystal plane is clearly observed in the selected area electron diffraction (SAED) and HRTEM, with an interplanar spacing of 0.246 nm. In contrast, for the ZP anode, a significant quantity of irregular grains is observed in Figure S11, predominantly consisting of crystal planes (100) and (101) with lattice spacings of ~ 0.232 and 0.214 nm, respectively. The preferential deposition of Zn(002) for the ZCBP anode is confirmed through *ex situ* XRD analysis after different plating durations. The peak intensity ratio ($I_{(002)}/I_{(101)}$) between the Zn(002) and Zn(101) planes increased from 0.35 (0 min) to 1.02 (80 min), indicating an increase in the deposition of Zn(002) on the ZCBP surface (Figure 4d). The deposition of Zn(002) is comparatively reduced in comparison to the ZP anode under identical conditions (Figure S12), which aligns with the findings from SEM and TEM analyses. Comparing SEM images of ZP and ZCBP after different stripping times, we observed that a significant number of pores gradually developed on the ZP electrode surface, whereas no notable changes were detected on the ZCBP electrode surface (Figure S13). This suggests that our prepared ZCBP anode can effectively resist electrical contact failure and suppress battery polarization during extended cycling. Besides, after stripping for 80 min, the ZP undergoes severe deformation, whereas the ZCBP experiences negligible deformation due to the structural support provided by carbon spheres (Figure S14). The deposition behavior of Zn^{2+} was directly observed through in situ optical microscopy, providing additional insights. The surface of ZP exhibits the formation of moss-like zinc within just 20 min after plating at a current density of 5 mA cm^{-2}, as illustrated in Figure 4e. Subsequently, the growth of moss-like zinc gradually intensifies accompanied by the generation of bubbles. As a stark contrast, the ZCBP surface displays uniform deposition of zinc metal under identical plating conditions, without any concurrent side reactions.

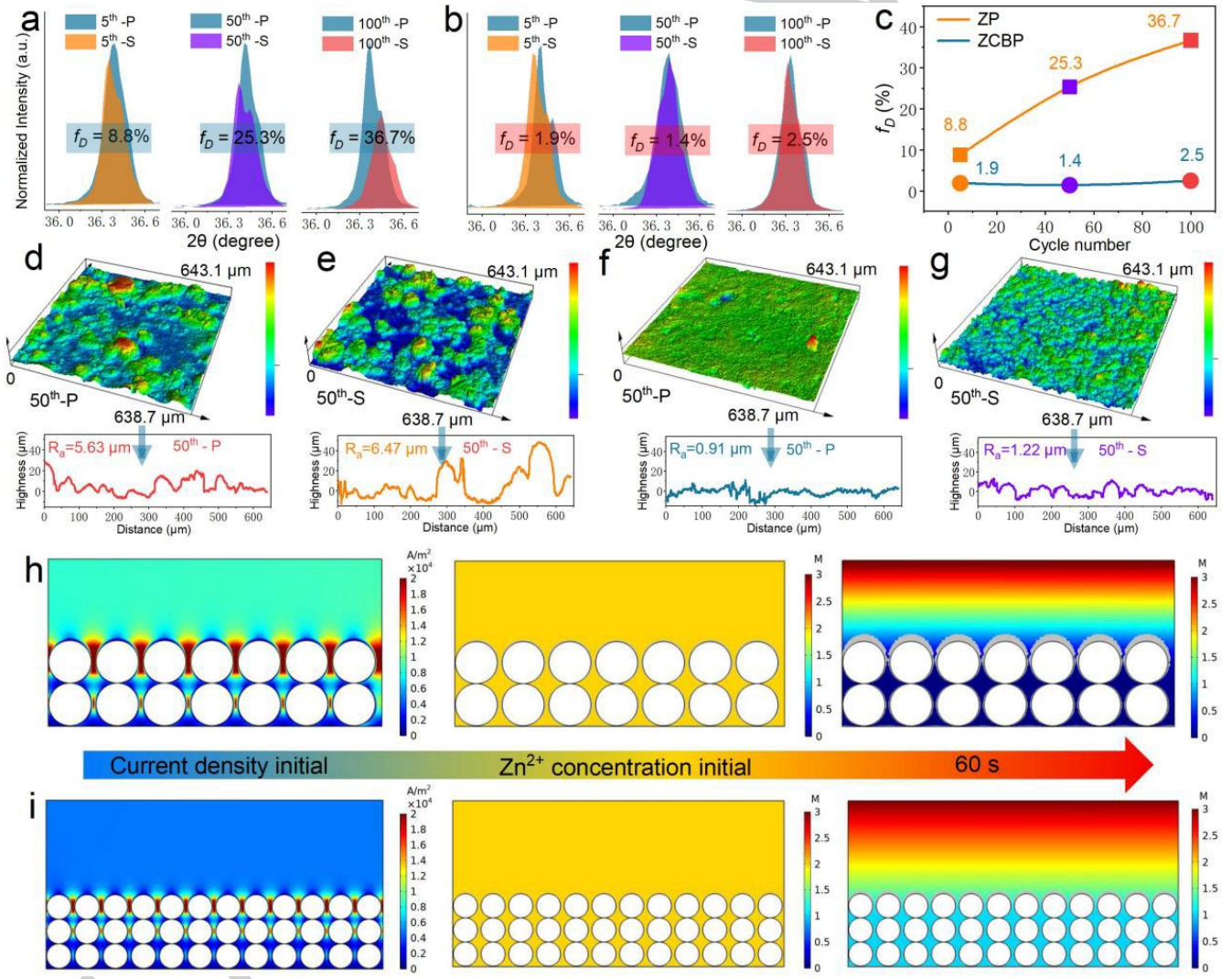

Figure 5. Enlarged XRD patterns of the **a)** ZP and **b)** ZCBP anodes obtained from parallelly cycled. **c)** evolution of the f_D factor. CLSM images and the corresponding surface roughness curves of the **d,e)** ZP and **f,g)** ZCBP anodes after 50 cycles. COMSOL simulation of current density distribution, and Zn^{2+} concentration and morphology evolution of the **h)** ZP and **i)** ZCBP anodes during plating.

The internal mechanism of Zn-oriented deposition was thoroughly investigated through the utilization of DFT calculation method, and the E_{ads} values for Zn atoms forming crystal planes of Zn(100) and Zn(002) on Bi are precisely computed. The E_{ads} of the (002) crystal plane (-20.01 kcal mol^{-1}) surpasses that of the (100) crystal plane (-12.19 kcal mol^{-1}), indicating a higher affinity for Zn adsorption on Bi in an ordered arrangement resembling the (002) crystal plane, thereby promoting directional growth of deposited Zn along this orientation (Figure 4f). Furthermore, the cyclic process of ZP and ZCBP anodes was evaluated by in situ Raman. The Zp electrode detects a progressively strengthening peak at ~ 465 cm^{-1} (Figure 4g), corresponding to the presence of the $(Zn(OH)_4)^{2-}$ in Raman spectrum.[26] In contrast, the surface of the ZCBP electrode exhibits no discernible side reactions throughout battery cycling (Figure 4h), thereby further substantiating the advantage of the ZCBP anode in suppressing dendrite formation and undesired secondary reactions. To further analyze the change in orientation of zinc growth on ZP and ZCBP electrodes, we introduce a deviation factor (f_D), and the detailed formula is provided in the supporting information. Ideally, in the absence of any side reactions, f_D should approach 0 %, signifying flawless alternation between plating and stripping processes.[27] A smaller f_D implies controlled and uniform zinc deposition, whereas a larger f_D indicates random deposition with a change in orientation, resulting in the continuous accumulation of zinc dendrites. To evaluate the deposition process of ZP and ZCBP anodes, f_D values were obtained by Zn plating/stripping from different cycles. The f_D of ZP//ZP symmetric cells increases with the extension of cycle time, as illustrated in Figure 5a,b and Figure S15. In contrast, the f_D values for ZCBP//ZCBP symmetric cell anodes are comparatively smaller, revealing a high level of reversibility for ZCBP anodes, as summarized in Figure 5c. In addition, the confocal laser scanning microscopy (CLSM) images of the ZP electrode after 50 cycles reveal a significant presence of protrusions, resulting in a roughened surface texture. The average surface roughness for plating and stripping surfaces measures 5.63 and 6.47 μm, respectively (Figure 5d,e). In stark contrast, the ZCBP effectively guides the homogeneous deposition of zinc, resulting in a smooth surface with an average roughness of 0.91 and 1.22 μm on the plating and stripping surfaces, respectively (Figure 5f,g).

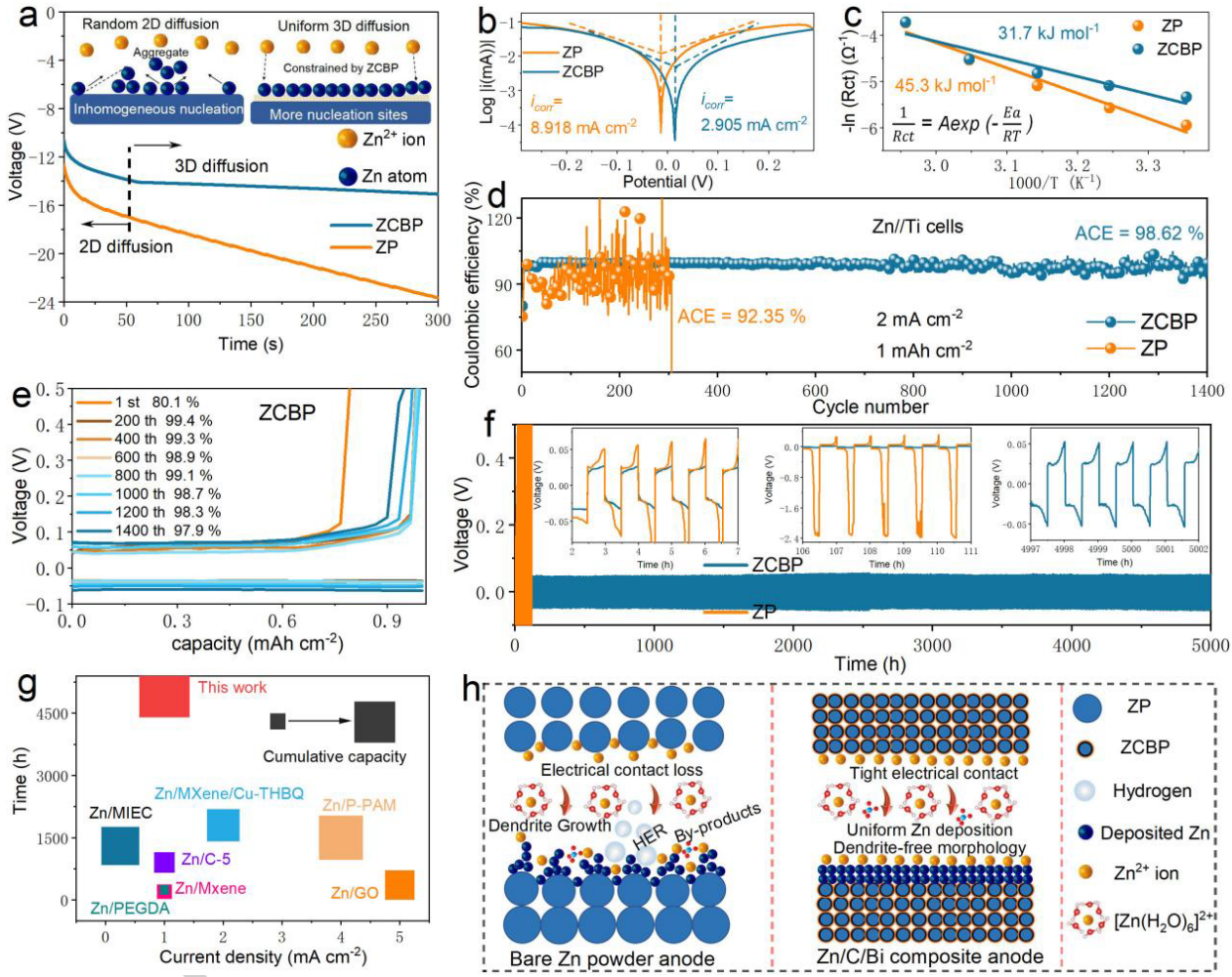

Figure 6. a) Chronoamperograms of the ZP and ZCBP anodes at an overpotential of –150 mV. Insets: types of Zn^{2+} diffusion and reduction processes. **b)** Tafel corrosion curves of ZP and ZCBP anodes in various electrolytes. **c)** Arrhenius curves and activation energies of the ZP and ZCBP anodes. **d)** CE plots of ZP//Ti and ZCBP//Ti cells at 2 mA cm^{-2}/1 mA h cm^{-2} and **e)** corresponding voltage profiles of ZCBP//Ti cells at various cycles. **f)** Galvanostatic charge/discharge cycling voltage profiles of ZP//ZP and ZCBP//ZCBP cells at 1 mA cm^{-2}/0.5 mA h cm^{-2}. **g)** Comparison of cyclic reversibility obtained in this work and previous studies. h) Schematic illustration of Zn plating/stripping behaviors for the ZP and ZCBP anodes.

To further reveal the difference of deposition behavior between ZP and ZCBP anodes, the electrodeposition model was utilized in COMSOL Multiphysics to simulate the evolution of surface, distribution of current density and concentration of Zn^{2+} (Figure S16). Due to the large size and poor electrical contact of ZP, charge accumulation occurs around the protrusions, leading to the formation of multiple sites with high current density (Figure 5h), thereby facilitating the non-uniform internal diffusion of Zn^{2+}. In contrast, the charge distribution within the ZCBP electrode is uniformly distributed, and there is no discernible concentration gradient (Figure 5i), thus ensuring a homogeneous deposition of zinc metal across the entire electrode, consitent with the above experimental characterization results.

The nucleation and deposition behavior of zinc anodes were investigated using Chronoamperometry (CA). The current density of ZP and ZCBP electrodes exhibits a progressive increase over the initial 50 s, indicating an extensive and prolonged 2D diffusion process (Figure 6a). For the ZP anode, the current density exhibits a continuous increase over the initial 50 s, indicating an uncontrolled and extensive 2D diffusion process characterized by the well-documented "tip effect". In this phenomenon, Zn^{2+} tend to migrate laterally across the Zn surface and accumulate at regions of high surface energy, particularly at the tips. This accumulation leads to the formation of larger particles in an attempt to minimize surface energy, ultimately resulting in dendrite formation. In a sharp contrast, a transient 2D diffusion phenomenon is observed, which is influenced by a long-standing 3D diffusion process occurring in the ZCBP anode, resulting in a steady and lower current density. This indicates that the lateral 2D diffusion of Zn^{2+} is effectively constrained, while 3D diffusion dominates during the initial nucleation process to promote homogeneous crystal growth. These findings further confirm that the ZCBP anode significantly enhances the uniform and smooth deposition behavior of Zn. Moreover, the corrosion current densities of the ZP and ZCBP electrodes in the 3 M $ZnSO_4$ electrolyte are 8.918 and 2.905 mA cm^{-2}, respectively (Figure 6b). After immersing ZP and ZCBP in the electrolyte for a week, a significant abundance of by-products can be visibly observed on the surface of the ZP electrode, whereas the surface of ZCBP appears comparatively smooth (Figure S17). In addition, the activation energy (E_a) of the reaction can serve as an indicator for both the complexity of the chemical process and the transport capacity of Zn^{2+}, as determined from electrochemical impedance spectroscopy (EIS) curves collected at different temperatures (Figure S18). The ZP electrode exbihits an E_a value of approximately 45.3 kJ mol^{-1} (Figure 6c), which significantly surpasses that of the ZCBP electrode (31.7 kJ mol^{-1}), implying that the ZCBP can deliver a commendable rate capability.

The ZP and ZCBP electrodes were employed to construct Zn//Ti cells for investigating the reversibility of plating/stripping processes. The ZP//Ti cells exhibit a limited lifespan, maintaining only 300 cycles, whereas the ZCBP//Ti cells demonstrate an average CE of 98.62 % over 1400 cycles (Figure 6d,e and Figure S19). It has been observed that the CE of Zn//Ti cells cycled in electrolytes surpasses 100%, attributed to the accumulation of zinc deposited on the ZP electrode. In each cycle, not all of the zinc deposited on the ZP electrode can be fully stripped back into the electrolyte, leading to the formation of "dead zinc." This phenomenon results in overcharging and consequently elevates the CE above 100%. Additionally, the ZCBP//ZCBP cells exhibit stable cycling for over 5,000 h at a current density of 1 mA cm^{-2} and a capacity of 0.5 mAh cm^{-2} during long-term galvanostatic cycling (Figure 6f), whereas the ZP//ZP cells undergo abrupt degradation within just 80 h. The sudden voltage drop may be attributed to a rapid temperature increase, as elevated temperatures expedite the transfer of Zn^{2+} and diminish the battery's overpotential. Even under deep discharge conditions (5 mA cm^{-2} and 2.5 mAh cm^{-2}), the ZCBP//ZCBP cells achieve a continuous operation time of over 900 h, while the ZP//ZP cells experience severe polarization and ultimately fails after only 30 h (Figure S20). A slight loss of electrical contact increases the voltage polarization of the symmetric cell, which is attributed to the loss of zinc metal due to the formation of inevitable by-products. In addition, the accumulation of by-products on the surface of the zinc anode can decrease the migration rate of Zn^{2+}, consequently leading to a progressive rise in polarization voltage. Besides, the XRD patterns show that even after 200 h of cycling at 5 mA cm^{-2}/2.5 mAh cm^{-2} (Figure S21), the ZCBP electrode surface still maintains the same characteristic metal peak observed initially, with fewer by-products present. In contrast, the diffraction peak of the by-product ($Zn_4SO_4(OH)_6{\cdot}xH_2O$) on the surface of the ZP electrode is significantly enhanced after cycling. These obtained results also provide direct evidence for the excellent structural integrity and stable surface texture of the prepared ZCBP anode. More importantly, the reasonably designed ZCBP electrode exhibits exceptional cyclic stability and surpasses the majority of current ZP-based aqueous batteries in performance (Figure 6g).[11,12,15,16,17,20,28] The chemical mechanism of ZP and ZCBP anodes during plating/stripping is illustrated in Figure 6h. For the ZP electrode, the outermost layer comprises zinc powder characterized by a high current density, which enhances the attraction of Zn^{2+} and primarily promotes their deposition on the external surface. Besides, a sequence of irreversible chemical reactions, including HER, corrosion, and dendrite growth, occurred during the process of zinc plating. The inevitable volume reduction during the stripping process is primarily attributed to the dissolution of zinc, which predominantly impacts the zinc powder in immediate proximity to the current collector. Following multiple cycles, the internal structure of the zinc powder deteriorates, leading to an increase in overpotential, loss of zinc powder, and subsequent failure of the battery. As for the ZCBP electrode, confined and cross-linked carbon spheres can facilitate electron transport across numerous continuous interfaces, thereby effectively mitigating volume expansion during repeated plating/stripping processes. Furthermore, the Bi nanosheets, characterized by their high adsorption capacity for Zn^{2+}, are uniformly anchored onto the surfaces of ZCP and ZP, functioning as preferred sites for zinc nucleation. This arrangement facilitates the regulation of the electric field distribution on the electrode surface. Consequently, these findings indicate a robust electrical contact and uniform deposition of Zn^{2+} along the Zn(002) crystal plane, thus maintaining the structural integrity of the electrode and preventing dendrite formation or collapse.

The stable and durable ZCBP anode with excellent cyclic stability provides significant advantages for the development of high-performance ZMABs. As a proof of concept, we demonstrated the integration of ZCBP anode with CNT@MnO_2 cathode to fabricate a full coin cell. The amorphous CNT@MnO_2 composite was synthesized through the co-thermal decomposition of a manganese acetate solution and oxidized carbon nanotubes (CNTs).[25] The SEM and energy-dispersive X-ray spectroscopy (EDS) images of the resulting amorphous CNT@MnO_2 are presented in Figure S22. The

ZCBP//CNT@MnO_2 cells display the smaller polarization and improved storage kinetics compared to the ZP//CNT@MnO_2 cells (Figure 7a). The cyclic voltammetry (CV) curves of the ZP//CNT@MnO_2 and ZCBP//CNT@MnO_2 cells exhibit distinct redox peaks within a scan rate range of 0.1 to 1 mV s^{-1} (Figure S23). The capacitance properties of ZP//CNT@MnO_2 and ZCBP//CNT@MnO_2 cells are shown in Figure S24. The *b* values for peak 1, peak 2, peak 3, and peak 4 are determined as 0.49, 0.64, 0.53, and 0.73 respectively, revealing that the reactions associated with these peaks are primarily governed by a combination of both ion diffusion and capacitive behavior (with capacitive behavior being predominant), which suggests that the utilization of ZCBP anode can effectively enhance the reaction kinetics within the battery. The CV curves and shaded areas of two coin cells are depicted in Figure S25. Notably, the capacitance contribution rates of the ZCBP//CNT@MnO_2 cells surpass those of the ZP//CNT@MnO_2 cell across all scan rates (Figure 7b,c). The higher capacitance contribution can be attributed to the promotion of efficient electron/ion migration by the ZCBP anode, thereby enabling excellent cyclic performance at high current densities. In addition, the ZCBP//CNT@MnO_2 cells deliver lower resistance compared to the ZP//CNT@MnO_2 cells, as evidenced by EIS analysis (Figure S26), thus further confirming the enhanced kinetics of ZCBP anodes. [29,30]

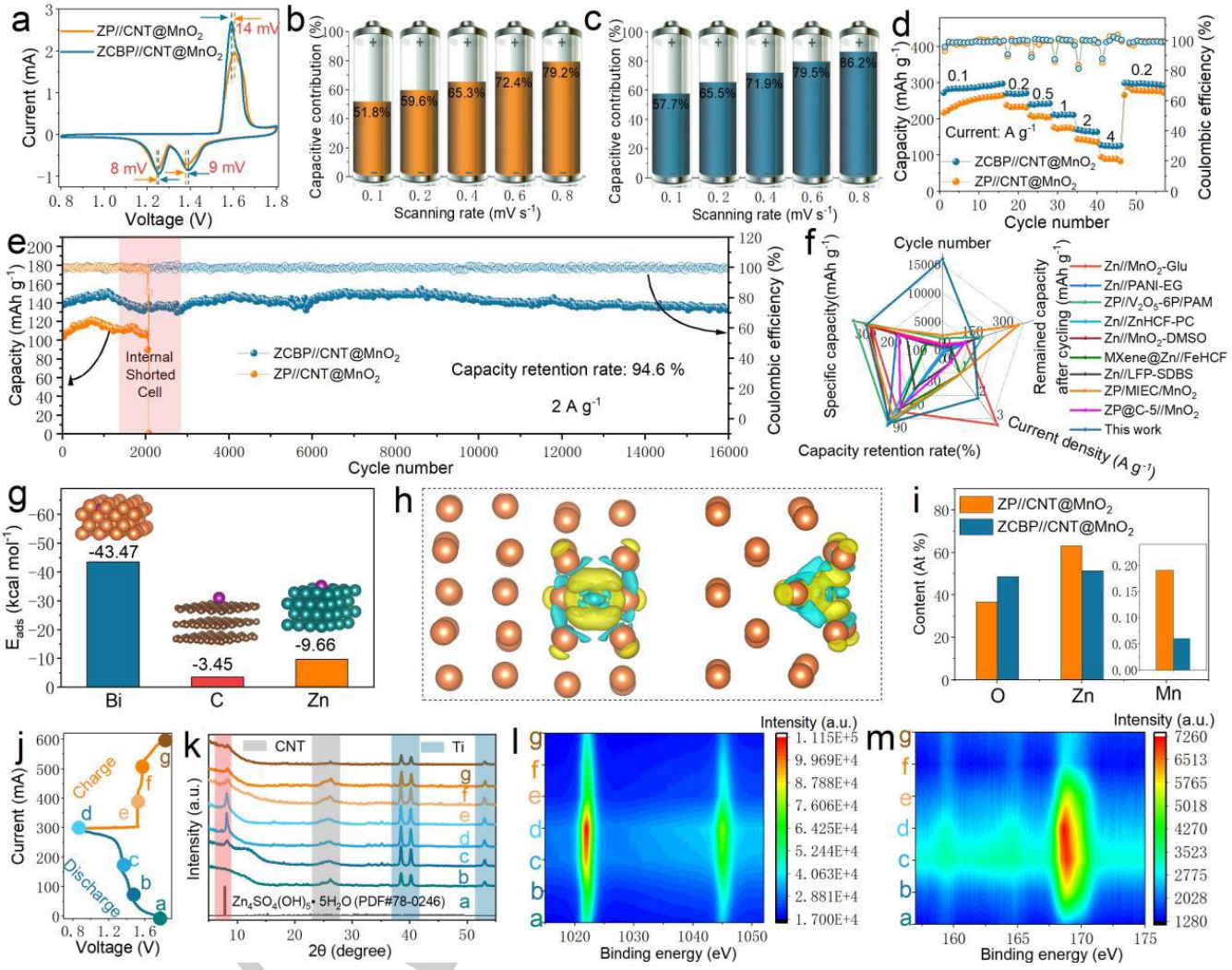

Figure 7. a) CV curves of the ZP//CNT@MnO_2 and ZCBP//CNT@MnO_2 cells. Comparison of capacitive contributions for the **b)** ZP//CNT@MnO_2 and **c)** ZCBP//CNT@MnO_2 cells. **d)** Rate performance of ZP//CNT@MnO_2 and ZCBP//CNT@MnO_2 cells. **e)** Capacity retention of ZP//CNT@MnO_2 and ZCBP//CNT@MnO_2 cells at a current density of 2 A g^{-1}. **f)** Comparison between the achieved performance in this study and the results documented for other aqueous batteries. **g)** Binding energies of Bi-Mn, C-Mn and Zn-Mn and the corresponding structures. **h)** The charge density difference of Bi-Mn (clusters with a semi-transparent yellow hue indicate an elevation in electron density, while those with a blue shade suggest a reduction). **i)** EDS results of the Zn anode for the ZP//CNT@MnO_2 and ZCBP//CNT@MnO_2 cells after 1000 cycles. **j, k)** ex-situ XRD patterns and 2D contour image of **l)** Zn 2p and **m)** S 2p at selected states.

The rate performance of full cells at different current densities (0.1, 0.2, 0.5, 1, 2 to 4 A g^{-1}) is displayed in Figure 7d. The ZCBP//CNT@MnO_2 cells exhibit a higher specific capacity and demonstrate faster response upon returning to the initial state of current density. Under various current densities, the charging and discharging curves of the ZCBP//CNT@MnO_2 cells show similarities with distinct

charging and discharging platforms along with enhanced specific capacity (Figure S27). Moreover, the self-discharge behavior of the two fully charged batteries is also compared (Figure S28). After a rest period of 36 h, the ZCBP//CNT@MnO_2 cells retain 86.2 % of the original capacity, which is higher than that of ZP//CNT@MnO_2 cells (61.3 %), indicating that the ZCBP anode achieves superior anti-corrosion ability. Excitingly, when the negative/positive (N/P) electrode capacity ratio is fixed to 15.97, the ZCBP//CNT@MnO_2 cells achieve excellent cycling stability (capacity retention rate of 94.6 %), maintaining more than 16,000 cycles at the current density of 2 A g^{-1} while delivering a satisfactory reversible capacity of 136.1 mAh g^{-1} (Figure 7e). In contrast, the bare ZP//CNT@MnO_2 cells exhibit rapid capacity degradation and only deliver a capacity of 0.8 mAh g^{-1} after 2067 cycles, possibly due to the electrical contact loss and dendrite growth of ZP anode. Furthermore, to evaluate the efficacy of the device, we also conducted a comparative analysis on the cyclic stability of the full coin cells at low current and N/P ratio conditions (0.2 A g^{-1} and N/P=10.65). The ZCBP//CNT@MnO_2 cells achieve a capacity retention rate of 97 % after 100 cycles, while maintaining a specific capacity of 301.2 mAh g^{-1} (Figure S29). The prepared ZCBP//CNT@MnO_2 cells provide significantly improved cyclic stability compared to the majority of previously reported high-energy aqueous batteries (Figure 7f).[11,16,20,28,31-35]

The deposition behavior of Mn^{2+} by ZCBP anode and the storage mechanism of CNT@MnO_2 were further investigated through a series of experimental and theoretical characterizations. The binding energy results clearly indicate that the E_{ads} of Mn^{2+}-Zn, Mn^{2+}-C, and Mn^{2+}-Bi are −9.66, −3.45, and −43.47 kcal mol^{-1}, respectively (Figure 7g). The findings indicate that the ZCBP exhibits a comparable and robust adsorption capacity towards Mn^{2+}, akin to its effect on Zn^{2+}, thereby facilitating the attainment of homogeneous Mn^{2+} deposition. Furthermore, the interfacial charge density differences (Figure 7h) calculations were employed for the analysis of surface atom charge transfer. The electron transfer from Mn^{2+} to Bi atoms is clearly observed, providing evidence for the presence of strong chemisorption that controls the homogeneous deposition of Mn^{2+}. To support the theoretical result, the effectiveness of ZCBP was further demonstrated by SEM and EDS mapping images on the surface of the Zn anode after 1,000 cycles of ZCBP//CNT@MnO_2 and ZP//CNT@MnO_2 cells. The anode surface of ZP//CNT@MnO_2 cells exhibites the presence of Zn/Mn dendrites, while that of ZCBP//CNT@MnO_2 cells displays a smooth and dendrite-free morphology (Figure S30). As summarized in Figure 7i, the concentration of Mn on the anode surface of ZP//CNT@MnO_2 cells is three times higher than that of ZCBP//CNT@MnO_2 cells, indicating a uniform deposition of Mn^{2+} by ZCBP, which aligns with the previous theoretical findings. Additionally, the reaction mechanism of the CNT@MnO_2 cathode was investigated through *ex situ* XRD and XPS characterization at selected states during the charge/discharge process (Figure 7j). The XPS spectra of Zn 2p and S 2p (Figure 7l,m) reveal a gradual increase in the signal intensity of Zn and S during the discharge process, suggesting a progressive deposition of related compounds containing Zn and S. Besides, the $Zn_4SO_4(OH)_5{\cdot}5H_2O$ phase was detected at a discharge voltage of 1.45 V. However, distinct flaky products were observed in both XRD and SEM results after discharging to 0.8 V (Figure 7k and Figure S31). The formation of $Zn_4SO_4(OH)_5{\cdot}5H_2O$ suggests that the co-insertion of H^+ and Zn^{2+} occurs at CNT@MnO_2 during the discharge process from 1.45 to 0.8 V.[36,37] After being charged to 1.5 V, the XRD peaks corresponding to $Zn_4SO_4(OH)_5{\cdot}5H_2O$ disappear, while the XPS peaks corresponding to $Zn_4SO_4(OH)_5{\cdot}5H_2O$ recover their original strength, revealing a reversible extraction of Zn^{2+} and H^+. Moreover, in the Mn 2p spectrum (Figure S32), the relative abundance of Mn^{4+} decreases while that of Mn^{3+} increases during discharge from 1.8 to 0.8 V. Conversely, when charged to 1.7 V, the ratio of Mn^{4+} and Mn^{3+} content remains similar to that at 1.8 V. Moreover, in the O 1s spectrum (Figure S33), the O-H region exhibits its maximum area at 0.8 V, whereas the Mn-O region contracts due to the co-insertion of H^+ and Zn^{2+}. Therefore, during the charging and discharging of ZCBP//CNT@MnO_2 cells, the improvement in single-electron reduction (Mn^{4+}) facilitates the storage of both Zn^{2+} and H^+ in the CNT@MnO_2 cathode, thus providing a stable and highly efficient energy source for the battery device.

Conclusions

In summary, we designed a stabilized three-tiered golf anode through the powder sherardizing and liquid phase reduction strategy. This unique three-tiered anode not only provides a multitude of uninterrupted interfaces to facilitate efficient electron transfer, but also effectively enhances the reversibility of Zn and Mn metals during repeated plating/stripping processes. Additionally, the golf anode can deliver enhanced Gibbs free energy and significant adsorption energy between bismuth nanosheets and Zn^{2+}, inhibiting HER while reducing the transport barrier for Zn^{2+} in the electrochemical process. Consequently, the Zn(002) crystal plane is preferentially deposited onto the surface of ZCBP, effectively inhibiting the formation of zinc dendrites. Benefitting from the above multi-functional role, the as-fabricated ZCBP symmetric cells exhibit excellent cyclic stability of 5,000 h and an ultrahigh CPC of 5 Ah cm^{-2} at 1 mA cm^{-2}/0.5 mAh cm^{-2}. Even under deep discharge conditions, the ZCBP//ZCBP cells achieve a continuous operation time of over 900 h at 5 mA cm^{-2}/2.5 mAh cm^{-2}. Furthermore, the ZCBP//CNT@MnO_2 cells achieve ultralong cycle life with a capacity retention of 94.6 % at 2 A g^{-1} after 16,000 cycles. More encouragingly, the ZCBP//CNT@MnO_2 cells demonstrate a remarkable capacity retention of 97.0% and maintain a specific capacity of 301 mAh g^{-1} even after undergoing 100 cycles at 0.2 A g^{-1}, thus ensuring the practicality and efficacy of the devices. The structural design of three-tiered golf anode can provide a novel approach for the utilization of ZMABs.

Acknowledgements

This work was financially supported by the Outstanding Talent Introduction Project of University of Electronic Science and Technology of China (No. 08JC00303) and National Postdoctoral Program for Innovative Talents (No. BX20240062). This work was also supported by the Sichuan Fuhua New Energy High-Tech Co., Ltd, postcode (621006) and the Research Grants Council of Hong Kong (RGC Postdoctoral Fellowship Scheme, Grant No.: PDFS2122-5S03).

Keywords: anode design · electrical contact · dendrite-free · dendrite-free · Zn-Mn aqueous batteries

[1] J. Zheng, Q. Zhao, T. Tang, J. Yin, C. D. Quilty, G. D. Renderos, X. Liu, Y. Deng, L. Wang, D. C. Bock, C. Jaye, D. Zhang, E. S.

Takeuchi, K. J. Takeuchi, A. C. Marschilok, L. A. Archer. *Science*. **2019**, *366*, 645–648.

[2] Q. Li, A. Chen, D. Wang, Y. Zhao, X. Wang, X. Jin, B. Xiong, C. Zhi, *Nat. Commun*. **2022**, *13*, 3699.

[3] J. Yang, X. Zhao, W. Zhang, K. Ren, X. Luo, J. Cao, S. Zheng, W. Li, X. Wu, *Angew. Chem*. **2023**, *135*, e202300258.

[4] T. Fang, M. Wu, F. Lu, Z. Zhou, Y. Fu, Z. Shi, *Energy Mater*. **2024**, *4*, 400039.

[5] B. Li, K. Yang, J. Ma, P. Shi, L. Chen, C. Chen, X. Hong, X. Cheng, M. Tang, Y. He, F. Kang, *Angew. Chem. Int. Ed*. **2022**, *61*, e202212587.

[6] F. Wang, O. Borodin, T. Gao, X. Fan, W. Sun, F. Han, A. Faraone, J. Dura, K. Xu, C. Wang, *Nat. Mater*. **2018**, *17*, 543−549.

[7] Z. Liu, Y. Huang, Y. Huang, Q. Yang, X. Li, Z. Huang, C. Zhi, *Chem. Soc. Rev*. **2020**, *49*, 180−232.

[8] B. Tang, L. Shan, S. Liang, J. Zhou, Energy Environ. Sci. *Energy Environ. Sci*. **2019**, *12*, 3288−3304.

[9] V. Yufit, F. Tariq, D. S. Eastwood, M. Biton, B. Wu, P. D. Lee, N. P. Brandon, *Joule*. **2019**, *3*, 485−502.

[10] J. F. Parker, C. N. Chervin, E. S . Nelson, D. R. Rolison, J. W. Long, *Energy Environ. Sci*. **2014**, *7*, 1117−1124.

[11] M. Zhang, P. Yu, K. Xiong, Y. Wang, Y. Liu, Y. Liang, *Adv. Mater*. **2022**, *34*, 2200860.

[12] Q. Li, S. Tang, R. Luo, P. Wei, P. Chen, J. Cong, G. Liu, Z. Liu, Y. Gou, H. Wu, S. Sun, J. Han, Y. Shi, C. Fang, C. Yan, *Energy Storage Mater*. **2024**, *66*, 103229.

[13] Z. Yang, Q. Zhang, W. Li, C. Xie, T. Wu, C. Hu, Y. Tang, H. Wang, *Angew. Chem. Int. Ed*. **2023**, *62*, e202215306.

[14] Q. Hu, J. Hou, Y. Liu, L. Li, Q. Ran, J. Mao, X. Liu, J. Zhao and H. Pang, *Adv. Mater*., **2023**, *35*, 2303336.

[15] H. Lu, J. Hu, K. Zhang, J. Zhao, S. Deng, Y. Li, B. Xu, H. Pang, *Adv. Mater*. **2024**, *36*, 2309753.

[16] X. Li, Q. Li, Y. Hou, Q. Yang, Z. Chen, Z. Huang, G. Liang, Y. Zhao, L. Ma, M. Li, Q. Huang, C. Zhi, *ACS Nano*. **2021**, *15*, 14631−14642.

[17] W. Du, S. Huang, Y. Zhang, M. Ye, C. Li, *Energy Storage Mater*. **2022**, *45*, 465−473.

[18] H. Chen, W. Zhang, S. Yi, Z. Su, Z. Zhao, Y. Zhang, B. Niu, D. Long, *Energy Environ. Sci*. **2024**, **17**, 3146–3156.

[19] H. Lu, J. Hu, Y. Zhang, K. Zhang, X. Yan, H. Li, J. Li, Y. Li, J. Zhao, B. Xu, *Adv. Mater*. **2023**, *35*, 2209886.

[20] J. Wang, H. Zhang, L. Yang, S. Zhang, X. Han, W. Hu, *Angew. Chem. Int. Ed*. **2024**, *63*, e202318149.

[21] J. Yang, X. Xu, Y. Gao, Y. Wang, Q. Cao, J. Pu, F. Bu, T. Meng, C. Guan, *Adv. Energy Mater*. **2023**, *13*, 2301997.

[22] R. Zhao, X. Dong, P. Liang, H. Li, T. Zhang, W. Zhou, B. Wang, Z. Yang, X. Wang, L. Wang, Z. Sun, F. Bu, Z. Zhao, W. Li, D. Zhao, D. Chao, *Adv. Mater*. **2023**, *35*, 2209288.

[23] X. Xie, S. Liang, J. Gao, S. Guo, J. Guo, C. Wang, G. Xu, X. Wu,G. Chen, J. Zhou, *Energy Environ. Sci*. **2020**, *13*, 503.

[24] T. Huang, K. Xu, N. Jia, L. Yang, H. Liu, J. Zhu, and Q. Yan, *Adv. Mater*. **2023**, *35*, 2205206.

[25] X. Zhang, J. Li, K. Qi, Y. Yang, D. Liu, T. Wang, S. Liang, B. Lu, Y. Zhu and J. Zhou, *Adv. Mater*. **2022**, *34*, 2205175.

[26] J. Zhou, M. Xie, F. Wu, Y. Mei, Y. Hao, L. Li, R. Chen, *Adv. Mater*. **2022**, *34*, 2106897.

[27] S. Wang, Z. Huang, J. Zhu, Y. Wang, D. Li, Z. Wei, H. Hong, D. Zhang, Q. Xiong, S. Li, Z. Chen, N. Li, C. Zhi, *Adv. Mater*. **2024**, *36*, 2406451.

[28] H. Wang, W. Wei, X. Liu, S. Xu, Y. Dong, R. He, *Energy Storage Mater*. **2023**, *55*, 597−605.

[29] X. Zhao, X. Wang, Z. Gu, J. Guo, J. Cao, Y. Liu, J. Li, Z. Huang, J. Zhang, X. Wu, *Adv. Funct. Mater*. **2024**, *34*, 2402447.

[30] H. Liang, H. Liu, J Guo, X. Zhao, Z. Gu, J. Yang, X. Zhang, Z. Liu, W. Li, X. Wu, *Energy Storage Mater*. **2024**, *66*, 103230.

[31] L. Geng, J. Meng, X. Wang, C. Han, K. Han, Z. Xiao, M. Huang, P. Xu, L. Zhang, L. Zhou, L. Mai, *Angew. Chem. Int. Ed*. **2022**, *61*, e202206717.

[32] P. Sun, L. Ma, W. Zhou, M. Qiu, Z. Wang, D. Chao, W. Mai, *Angew. Chem. Int. Ed*. **2021**, *60*, 18247–18255.

[33] L. Cao, D. Li, E. Hu, J. Xu, T. Deng, L. Ma, Y. Wang, X. Yang, C. Wang, *J. Am. Chem. Soc*. **2020**, *142*, 21404−21409.

[34] X. Yang, Q. Zhou, S. Wei, X. Guo, P. Chimtali, W. Xu, S. Chen, Y. Cao, P. Zhang, K. Zhu, H. Shou, Y. Wang, X. Wu, C. Wang, L. Song, *Small Methods*. **2023**, *8*, 2301115.

[35] F. Ming, Y. Zhu, G. Huang, A. Emwas, H. Liang, Y. Cui, H. Alshareef, *J. Am. Chem. Soc*. **2022**, *144*, 7160−7170.

[36] F. Wan, L. Zhang, X. Dai, X. Wang, Z. Niu, J. Chen, *Nat. Commun*. **2018**, *9*, 1656.

[37] S. Deng, Z. Tie, F. Yue, H. Cao, M. Yao, Z. Niu, *Angew. Chem. Int. Ed*. **2022**, *61*, e202115877.

Table of Contents

Title: A Three-Tiered Golf Anode towards Ultralong-Life Zn-Mn Aqueous Batteries

A highly conductive and three-tiered golf anode was developed to simultaneously enhance the reversibility of Zn and Mn metals. The experiment characterizations and theoretical simulations demonstrate that the three-tiered golf anode is achieved by inner zinc powder, intermediate carbon and outer bismuth layer, which can effectively enhance the Gibbs free energy and mitigate the volume change of the anode.

ToC figure: